


SCIENTIFIC REPORTS



OPEN

Directional subradiance from helical-phase-imprinted multiphoton states

H. H. Jen 

We theoretically investigate the far-field scattering properties of multiphoton super- and subradiant states which can be prepared by multiphoton excitations with orbital angular momentum (OAM). Due to multiphoton interference, the far-field patterns of the subradiant modes show directional scattering along the excitation direction or transverse scattering with number of peaks equal to the number of atoms. When more atoms are involved, we consider structures of stacked and concentric rings, which respectively show enhanced directional scattering and smoothed emission patterns. Our scheme gives insights to prepare many-body subradiant states, and is potentially applicable to quantum storage of multiphoton with OAM. By designing atomic spatial distributions, these cooperative states can tailor the far-field emission properties, which is useful for light collections and quantum information manipulations.

Superradiance^{1,2} results from cooperative light-matter interactions, which typically radiates directionally³ with a shortened time scale. This enhancement of the spontaneous emission comes from the resonant dipole-dipole interactions (RDDI)⁴ induced by rescattered photons between atoms. In such strong coupling regime, subradiance on the other hand also becomes evident⁵ in the afterglow⁶ of the superradiance. The remnant radiation with slow decay rates signifies the presence of subradiant states, and at the same time, indicates that the initially excited superradiant state is not the eigenstate of the dynamically interacting system. This is due to the long-range nature of RDDI which couples every other atom in the system, and thus in general all Hilbert space of super- and subradiant states are involved in the dissipation process. This offers an opportunity to manipulate light-matter interacting systems^{7,8} and to deterministically access these subradiant states, for example, in one-dimensional^{9–12}, two-dimensional (2D)¹³, or three-dimensional (3D) atomic arrays^{14,15} and 2D metamaterial^{16,17}. In addition to neutral atoms, subradiant states can also be excited and prepared in two trapped ions¹⁸, molecules^{19–21}, plasmonic nanocavities²², and atomic arrays in a cavity²³.

In addition to the obvious linewidth broadening (superradiance) along with cooperative frequency shifts^{24–29} or narrowing (subradiance)⁵ in fluorescence experiments, collective light scattering in a dense atomic medium^{30–32} also provides useful information of cooperative light-matter interacting systems. Aside from well-known directional light scattering of superradiance, recently we propose to use helical-phase-imprinted (HPI) single-photon subradiant states³³ on a ring array to investigate the far-field emission patterns. This subradiant state can be prepared by absorption of single-photon carrying the orbital angular momentum (OAM)^{34–38} and becomes the alternative candidate for storage of light quanta with OAM^{39–41}. Similar ring-shaped lattice has been proposed to excite high-lying Rydberg states⁴² which lead to nonclassical collective photon emissions.

In this paper, we investigate the far-field scattering properties of HPI multiphoton subradiant states in the ring arrays, which are less studied systematically. The HPI multiphoton states can tailor and modify the radiation properties by controlling and engineering the atomic configurations and light polarizations. Thus, this is potentially useful in generating and detecting entangled multiphoton states⁴³, and also offers opportunities in manipulating multiphoton resource in quantum network⁷.

Helical-phase-imprinted multiphoton states

When a resonant multiphoton source of M photons is absorbed by N two-level atoms ($|g\rangle$ and $|e\rangle$), a symmetric state can be formed, and such that M excited and $N - M$ ground states are symmetrically distributed in all atoms with equal probabilities $(C_M^N)^{-1}$ where C denotes the binomial coefficients. To access the other possible

Institute of Physics, Academia Sinica, Taipei, 11529, Taiwan. Correspondence and requests for materials should be addressed to H.H.J. (email: sappyjen@gmail.com)

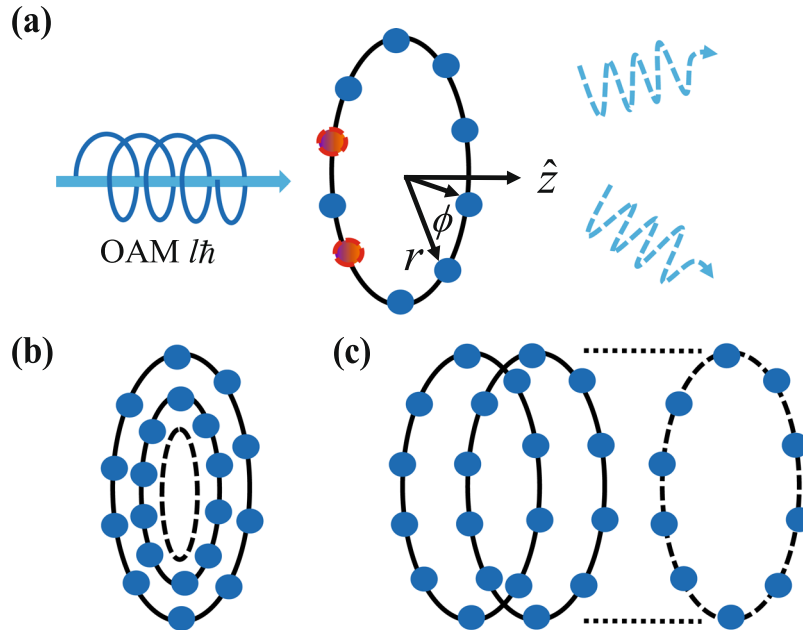


Figure 1. Schematic helical-phase-imprinted multiphoton state preparation. (a) A multiphoton source carrying orbital angular momentum (OAM) is absorbed by the atoms on a single ring, where two excitations (dash circles) are shown here for demonstration and as one possibility out of the complete excitation space. The atomic system is then prepared into one of multiphoton super- or subradiant states, depending on OAM $l\hbar$; of light. The scattered light property out of these multiphoton states depends on the ring geometry of radius r and ϕ . Other atomic configurations of (b) concentric or (c) stacked rings can be the candidates for creation of helical-phase-imprinted multiphoton states.

multiphoton super- and subradiant states, we have proposed to use phase-imprinting methods to unitarily transform the system into¹⁵,

$$|\phi_n^{(M)}\rangle = \prod_{j=1}^M \sum_{\mu_j=\mu_{j-1}+1}^{N-M+j} \frac{e^{i\mathbf{k}_L \cdot \mathbf{R}_M}}{\sqrt{C_M^N}} e^{i\frac{2\pi}{C_M^N} [f(\vec{\mu})-1]} |\psi_N^{(M)}(\vec{\mu})\rangle, \tag{1}$$

where $n \in [1, C_M^N]$ and $f(\vec{\mu}) = \sum_{i=1}^M \mu_i$ indicates the linear increases of the imprinted phases in a 3D atomic array. We use a concise representation of the traveling phase $\mathbf{k}_L \cdot \mathbf{R}_M \equiv \mathbf{k}_L \cdot \sum_{m=1}^M \mathbf{r}_{\mu_m}$ and define the bare states with M excitations, $|\psi_N^{(M)}(\vec{\mu})\rangle \equiv |e\rangle_{\mu_1} |e\rangle_{\mu_2} \dots |e\rangle_{\mu_M} |g\rangle^{\otimes(N-M)}$ with $\vec{\mu} = (\mu_1, \mu_2, \dots, \mu_M)$. Note that this specific construction of Hilbert space is not unique, and there are many ways to create such multiple excitations space. This phase imprinting method dynamically controls the incrementally increasing phases either by Zeeman field or a Stark field gradient pulse, but demands large field gradient strengths or long interaction time.

Nevertheless, this linearly increasing phase can be also imprinted in an azimuthal direction by light with OAM³³ without external field gradients. We consider Laguerre-Gaussian modes of light excitations, which carries a phase dependence of $e^{il\phi}$ with a quantized OAM of $l\hbar$. For N_ϕ equidistant atoms sitting on a single ring in Fig. 1, the light imprints the phase of $\phi = 2\pi(\sum_{m=1}^M \mu_m - 1)/N_\phi$ on the atoms for M excitations. To label the ring structures of concentric or stacked rings in Fig. 1(b) and (c), we raise up atomic indices to superscripts and denote $\mu^j = (\mu_r^j - 1)N_\phi + \mu_\phi^j$ or $(\mu_z^j - 1)N_\phi + \mu_\phi^j$, respectively. The number of integrated rings is $\mu_r^j \in [1, N_{r,z}]$ where $N_{r,z}$ represents the rings along $\hat{r}(z)$ direction, and the total number of atoms becomes $N = N_{r,z}N_\phi$. For each atom labeled as j , μ_ϕ^j is within $[1, N_\phi]$. Therefore, the light with OAM absorbed by the ring array forms HPI multiphoton states

$$|\phi_t^{(M)}\rangle_{\text{HPI}} = \prod_{j=1}^M \sum_{\mu^j=\mu^{j-1}+1}^{N-M+j} \frac{e^{i\mathbf{k}_L \cdot \mathbf{R}_M^j}}{\sqrt{C_M^N}} e^{i\frac{2\pi}{N_\phi} [f^j(\vec{\mu}_\phi^j)-1]} |\psi_N^{(M)}(\vec{\mu})\rangle, \tag{2}$$

where here we note that $\vec{\mu}_\phi^j = (\mu_\phi^1, \mu_\phi^2, \dots, \mu_\phi^M)$ and define $\mathbf{R}_M^j \equiv \sum_{j=1}^M r_{\mu^j} f^j(\vec{\mu}_\phi^j) \equiv \sum_{j=1}^M \mu_\phi^j$. Here we propose to use Laguerre-Gaussian modes of $u_{p=0}^l(r, \phi)$ with an arbitrary OAM $e^{il\phi}$ and zero radial index (p) to prepare HPI multiphoton states. For more technical details on excitation and preparation of the states, we explain in Supplemental Information.

Comparing Eq. (1), the HPI multiphoton states of Eq. (2) has limited imprinted phases by OAM of light since it puts phases along $\hat{\phi}$ direction only. Thus, equation (2) forms only a subspace of multiply-excited states of equation (1). However, HPI multiphoton states can expedite the preparation protocols by simply using light with OAM, which removes the requirement of external addressing fields and makes the proposed scheme here more

efficient and dominant in generating multiphoton subradiant states. In the next subsection, we further derive the general expression for far-field emission properties of HPI multiphoton states, which we use to investigate the effect of multiphoton interference and atomic configurations on the emission patterns in the next section.

Far-field scattering. The far-field scattering patterns can provide a unique characterization of the HPI multiphoton states. The general expression of the far-field scattering from uniformly-polarized two-level atoms is⁴

$$\langle \vec{E}^*(\mathbf{R}, t') \vec{E}(\mathbf{R}, t) \rangle = \left(\frac{\omega_{eg}^2}{4\pi\epsilon_0 c^2} \right)^2 \frac{|\vec{p}|^2}{R^2} [1 - (\hat{\mathbf{R}} \cdot \hat{\mathbf{p}})^2] \sum_{\alpha, \beta=1}^N e^{i\mathbf{k}_R \cdot \mathbf{r}_{\alpha\beta}} \langle \hat{\sigma}_\alpha^+(t') \hat{\sigma}_\beta^-(t) \rangle, \quad (3)$$

where ω_{eg} is the energy difference, $\hat{\mathbf{R}}/\mathbf{k}_R$ denotes the observation direction, $\mathbf{r}_{\alpha\beta} = \mathbf{r}_\alpha - \mathbf{r}_\beta$ denotes mutual atomic separations, and the dipole orientation $\hat{\mathbf{p}}$ is determined by the polarization of excitation field. Since the far-field scattering concerns the observation point way distant from the atoms, the radiation phase is then contributed by the retarded ones $e^{-i\mathbf{k}_R \cdot \mathbf{r}_\alpha}$ and $|\mathbf{k}_R| = \omega_{eg}/c$. At equal time of equation (3), we obtain the far-field radiation patterns from the HPI multiphoton states $|\phi_l^{(M)}(t)\rangle_{\text{HPI}}$,

$$\begin{aligned} \Omega_f(\theta, \phi) &\equiv \frac{\langle \vec{E}^*(\mathbf{R}, t) \vec{E}(\mathbf{R}, t) \rangle}{I_0(t)}, \\ &= [1 - (\hat{\mathbf{R}} \cdot \hat{\mathbf{p}})^2] \prod_{m=1}^M \sum_{\mu^m=\mu^{m-1}+1}^{N-M+m} \prod_{j=1}^M \sum_{\mu^j=\mu^{j-1}+1}^{N-M+j} \frac{e^{i(\mathbf{k}_R - \mathbf{k}_l) \cdot (\mathbf{R}_M^m - \mathbf{R}_M^j)}}{C_M^N} e^{\frac{i2\pi}{N_\phi} [f^j(\vec{\mu}_\phi^j) - f^m(\vec{\mu}_\phi^m)]}, \end{aligned} \quad (4)$$

where $I_0(t)$ is the time-evolving fluorescence intensity and depends on the eigenvalues of the coupling matrix^{10,14,15}. The multiphoton coupling matrix elements from RDDI can be seen in Methods and ref.¹⁵. An implicit dependence of multiply-excited configurations is in the spatial and imprinted phases respectively. equation (4) characterizes the far-field scattering property from the HPI multiphoton states created by an excitation field with $l\hbar$ OAM, which involves the interplay of the atomic distributions \mathbf{r}_{μ^j} and the helical phases $\propto e^{i2\pi l N_\phi}$. In the next section, we investigate the far-field scattering properties for the atomic configurations in Fig. 1 and various OAM of light.

Light scattering from HPI multiphoton states

Here we focus on HPI two- and three-photon states prepared in a single, stacked, and concentric rings. For M excitations, there are in general C_M^N possible HPI multiphoton states. Before we investigate the case of many atoms, a few atoms study can illuminate the interplay between imprinted phases, atomic spatial distributions, and multiphoton interference.

Three- and four-atom case. For three atoms on a ring with the same arc length, we have the far-field scattering from HPI two-photon states from \hat{x} -polarized light,

$$\begin{aligned} \Omega_f(\theta, \phi) &= (1 - \sin^2 \theta \cos^2 \phi) \left\{ 3 + \left(e^{i\sqrt{3}\bar{r} \sin \theta \sin \phi + i\frac{2\pi}{3}} \right. \right. \\ &\quad + e^{i\frac{3}{2}\bar{r} \sin \theta \cos \phi + i\frac{\sqrt{3}}{2}\bar{r} \sin \theta \sin \phi + i\frac{4\pi}{3}} \\ &\quad \left. \left. + e^{i\frac{3}{2}\bar{r} \sin \theta \cos \phi - i\frac{\sqrt{3}}{2}\bar{r} \sin \theta \sin \phi + i\frac{2\pi}{3}} + c.c. \right) \right\}, \end{aligned} \quad (5)$$

where $\bar{r} = |\mathbf{k}_R|r$ and c.c. means the complex conjugate of counterparts in the parenthesis. This far-field pattern is exactly the same as HPI single photon states, since the traveling phases contributed from atomic configurations in equation (4), $\mathbf{R}_M^m - \mathbf{R}_M^j$, involve only pairwise atoms. This is also the case for the difference of imprinted helical phases, $f^j(\vec{\mu}_\phi^j) - f^m(\vec{\mu}_\phi^m)$. Therefore, the far-field patterns of HPI multiphoton states with $M = N - 1$ exactly correspond to HPI single photon states on a ring³³.

The unique emission pattern of HPI multiphoton states then emerges in two-photon states of a ring with four atoms. In Fig. 2, we show the scattering patterns $\Omega_f(\theta, \phi)$ with associated fluorescence intensity $I_0(t)$. Since the HPI multiphoton states are not the eigenstates of the system in general¹⁵, their fluorescence results from several eigen decay rates which we show in Fig. 2(c) for the specific atomic configuration with six (C_M^N) eigenstates. We then distinguish the sub- ($l = 1, 2$) from superradiant ($l = 4$) states by comparing $I_0(t)$ with the intrinsic decay function $e^{-2\Gamma t}$. A clear signature of the subradiant far-field pattern is the side scattering^{30,31,33} in the mode of $l = 1$, while the superradiant mode of $l = 4$ typically shows a forward and backward scattering along the excitation direction \hat{z} .

Interestingly, the most subradiant state of $l = 2$ shows not only small side scattering peaks at $\phi = \pi/2$ and $3\pi/2$, but also enhanced forward and backward scatterings, bearing both signatures of single-photon sub- and superradiance. This is in contrast to HPI single-photon subradiant states³³ which allow only side scatterings. In addition, this illustrates the multiphoton interference in the HPI states, which carries an extra degree of freedom in phase-imprinting other than atomic configurations (traveling phases) and excitation modes (various l). We note that discrete C_4 rotational symmetry in $\Omega_f(\theta, \phi)$ is preserved for linear polarizations in the atomic system of $N = 4n$ with integers n . This can be seen as we change ϕ to $\phi + \pi/2$ in the prefactor of equation (4), which changes

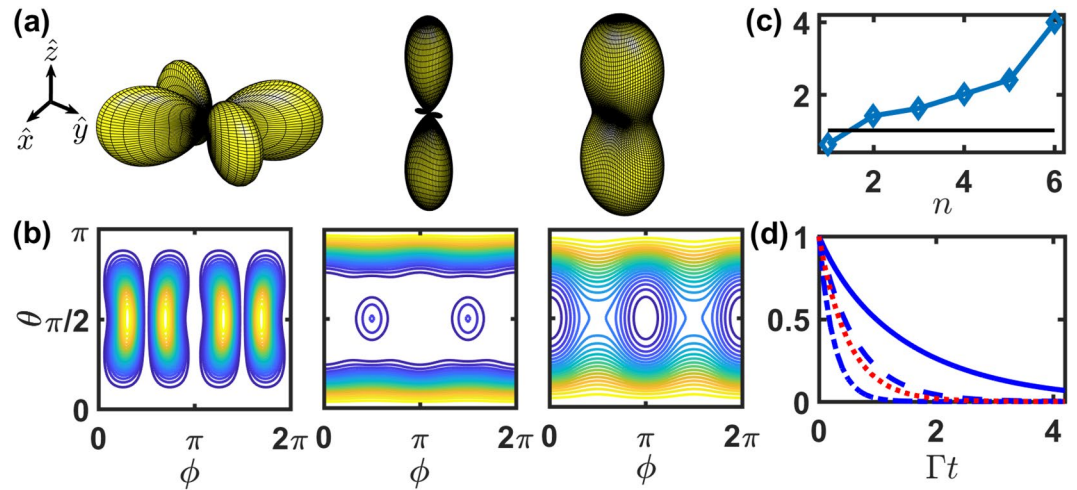


Figure 2. The far-field $\Omega_f(\theta, \phi)$ of \hat{x} -polarized HPI two-photon states for four atoms on a ring. (a) Three-dimensional plots of $\Omega_f(\theta, \phi)$ at $r/\lambda = 0.2$ with $l = 1, 2$ and 4 , respectively. Corresponding two-dimensional plots are shown in (b). (c) The spontaneous decay rates, $\text{Re}[-\lambda_n]/(\Gamma/2)$ in an ascending order, are numerically calculated from the eigenvalues λ_n for this given atomic configuration. A horizontal line guides the eye for natural decay rate $\text{Re}[-\lambda_n] = \Gamma/2$. (d) The fluorescence intensity $I_0(t)$ of the HPI two-photon states with $l = 1$ (dash), 2 (solid), and 4 (dash-dot), compares with $e^{-2\Gamma t}$ (dot).

\hat{x} -polarized emission pattern to \hat{y} -polarized one. Also $l \leftrightarrow -l$ symmetry in $\Omega_f(\theta, \phi)$ is sustained for all N as $r \rightarrow 0$. In general for all r , even N preserves this mode symmetry. This mode symmetry emerges due to the regular convex polygon geometry which we assume for atoms forming a ring and incremental helical phases we apply, and as such the far-field scattering in equation (4) does not change as $l \rightarrow -l$ (or equivalently $N - l$). Therefore, $\Omega_f(\theta, \phi)$ of $l = 3$ is the same as $l = 1$ in Fig. 2. For another example of $N = 6$ with $M = 2$, one of the far-field scattering contributions, $\cos[\mathbf{k}_R \cdot (\mathbf{r}_1 + \mathbf{r}_2 - \mathbf{r}_3 - \mathbf{r}_4) + 2l\pi \times 4/6]$, pairs up with $\cos[\mathbf{k}_R \cdot (\mathbf{r}_4 + \mathbf{r}_5 - \mathbf{r}_1 - \mathbf{r}_6) + 2l\pi \times (-2)/6]$, which interchanges to each other as $l \rightarrow -l$.

Single ring. Here We take $N = 12$ on a ring as an example and investigate the far-field scattering patterns of HPI two-photon subradiant states. This N has C_4 rotational symmetry so we use \hat{x} -polarized light without loss of generality. In Fig. 3(a1), we show the side scattering of the subradiant modes with $l = 3, 4$ and 5 . The specific two-dimensional plot of $l = 3$ mode is illustrated in Fig. 3(b), which reveals N side scattering peaks. This specific mode corresponds to the number of atoms, similar for $l = 1$ mode in Fig. 2(a) and thus can be used to characterize the atomic configuration. The $l = 6$ subradiant mode in Fig. 3(a1), also similar to the $l = 2$ mode in Fig. 2(a), shows forward and backward scattering, but radiates in a rate only second to the most subradiant mode of $l = 5$. This can be seen in the time evolutions of the subradiant modes in Fig. 3(c) where $l = 5$ state evolves longer than the other subradiant modes since it occupies the most subradiant eigen decay rate. The HPI states of $l = 3, 4$ and 5 drop rapidly initially due to partial overlaps with the superradiant eigenmodes while later they still evolve past the intrinsic decay $e^{-2\Gamma t}$, indicating a subradiant afterglow. In the insets of Fig. 3(c), we show the effect from the fluctuations of atomic positions along the arc length on the fluorescence intensity. The oscillation peaks at a later time are smoothed out as the fluctuation increases, and the fitted exponential decay rates ($e^{-\Gamma_f t}$) of the mean radiation envelopes are $\Gamma_f/\Gamma = 0.419, 0.655, 0.663$, respectively for free of, 5%, and 10% position fluctuations. This leads to the decrease of the effective lifetime of the HPI subradiant state, similar to the suppression of linewidth narrowing in the subradiant eigenmodes of 2D arrays with position fluctuations¹³. The averaged emission patterns are shown for $l = 3$ and 6 respectively in Fig. 3(a2) with 5% position fluctuations. The mode of $l = 3$ also shows the smoothing feature in the side peaks along with finite but less significant forward and backward scatterings, in contrast to Fig. 3(b) without position fluctuations. On the contrary for the mode of $l = 6$, the forward and backward scattering pattern is more resilient to the fluctuations. The clear side peaks of $l = 3$ can be restored as the fluctuation is reduced below around 1%.

For far-field scattering patterns of HPI three-photon subradiant states, we show in Fig. 4 with $N = 8$. We note that as N increases, the total Hilbert space goes up as $\mathcal{O}(N^3)$, so here we only focus on the feature of directional subradiance instead of multi-atom effect. For larger N on the other hand, we will investigate the effect of stacked and concentric rings in the next subsection. In Fig. 4, we show the effect of multiphoton interference on the far-field scattering, where the subradiant mode of $l = N/2$ encodes the information of N side scattering peaks, in contrast to forward/backward scattering $l = N/2$ modes in Figs 2 and 3. Furthermore, the subradiant mode at $l = 3$ in Fig. 4 shows an oblique scattering, instead of forward and backward directions.

The HPI multiphoton subradiant states show quite rich far-field scattering patterns. Except for side scatterings, the subradiant emission also allows along or near the excitation direction. In addition, the oscillation of time evolutions manifests the beating frequency from the differences of cooperative frequency shifts¹⁰. This shows flexibility to tailor and manipulate the emission time and directions of multiphoton states, and enables the one to one correspondence between the atomic configurations and the far-field scattering patterns.

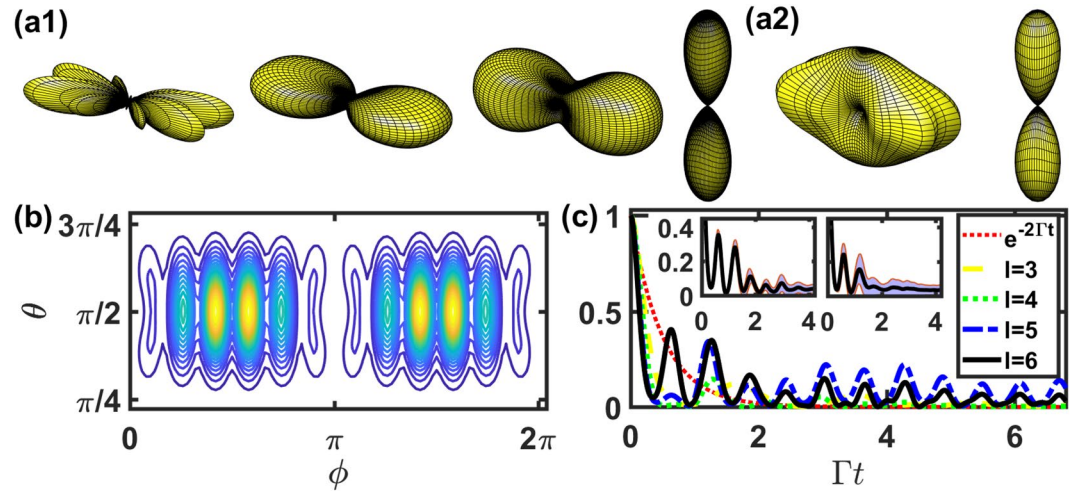


Figure 3. The far-field $\Omega_f(\theta, \phi)$ of \hat{x} -polarized HPI two-photon states for $N = 12$ on a ring. (a1) Three-dimensional plots of $\Omega_f(\theta, \phi)$ with $l = 3-6$ with a specific two-dimensional plot of $l = 3$ in (b). (a2) Averaged three-dimensional plots of $\Omega_f(\theta, \phi)$ with $l = 3$ and 6 , with 5% atomic position fluctuations. The viewing angle and r are the same as in Fig. 2(a). (c) The fluorescence intensity $I_0(t)$ of the HPI two-photon states for $l = 3-6$, compares with $e^{-2\Gamma t}$. The insets of (c) show the plot of $l = 6$ with fluctuations of atomic positions in the left and right, respectively with 5% and 10% uniformly distributed deviations around the fixed positions. The shaded areas represent 1σ standard deviation of the mean curve (solid).

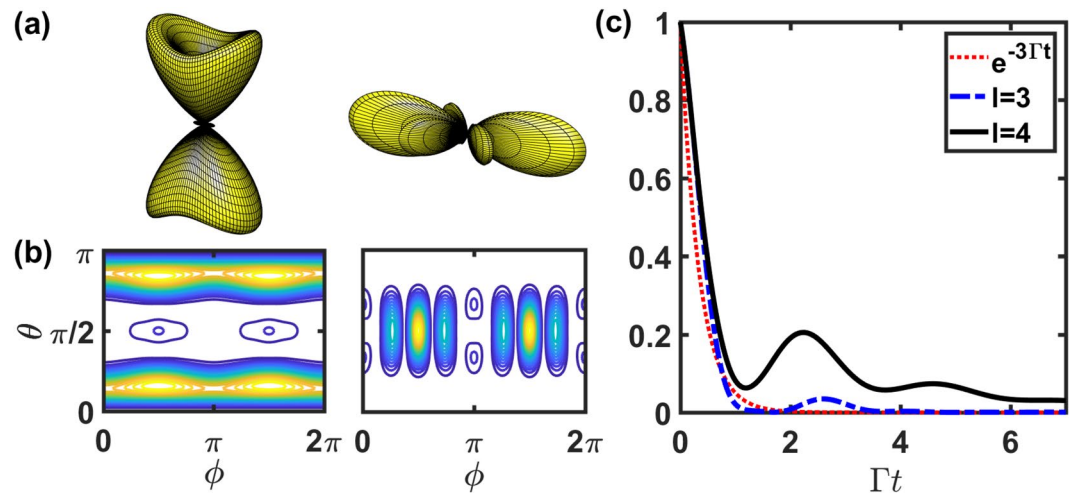


Figure 4. The far-field $\Omega_f(\theta, \phi)$ of \hat{x} -polarized HPI three-photon states for $N = 8$ on a ring. (a) Three-dimensional plots of $\Omega_f(\theta, \phi)$ of subradiant states with $l = 3$ and 4 . Corresponding two-dimensional plots are shown in (b). (c) The fluorescence intensity $I_0(t)$ of the HPI three-photon states with $l = 3$ and 4 , compares with $e^{-3\Gamma t}$. The viewing angle and other parameters are the same as in Fig. 2(a).

Stacked and concentric rings. Finally we investigate the far-field scattering properties of HPI multiphoton subradiant states in the stacked and concentric rings. We have investigated these two configurations of HPI single-photon states³³ which show enhanced forward scattering and narrowing effect on side scattering peaks in the stacked and concentric rings respectively. In Fig. 5, we show the far-field scattering properties of HPI two-photon subradiant states with $l = 2$ and 4 , in the stacked and concentric rings respectively. Similar to HPI single-photon states, the forward scattering is enhanced in Fig. 5(c) and (e) as N_z increases. On the contrary, comparing Figs 3(a) and 5(a), the transverse scattering peaks are smoothed out due to multiphoton interference. This smoothing effect is even more significant in the concentric rings of Fig. 5(d) as N_z increases, and the states of $l = 2$ and 4 become superradiant for a larger N_z . In Fig. 5(f), the effect of concentric rings weakens the forward-backward scattering along with emerging side scattering. Therefore, in the perspective of preparing multiphoton subradiant states in a large atomic system, the stacked rings are better than the concentric ones since the former allows a more directional emission pattern which is better for light collection and detection.

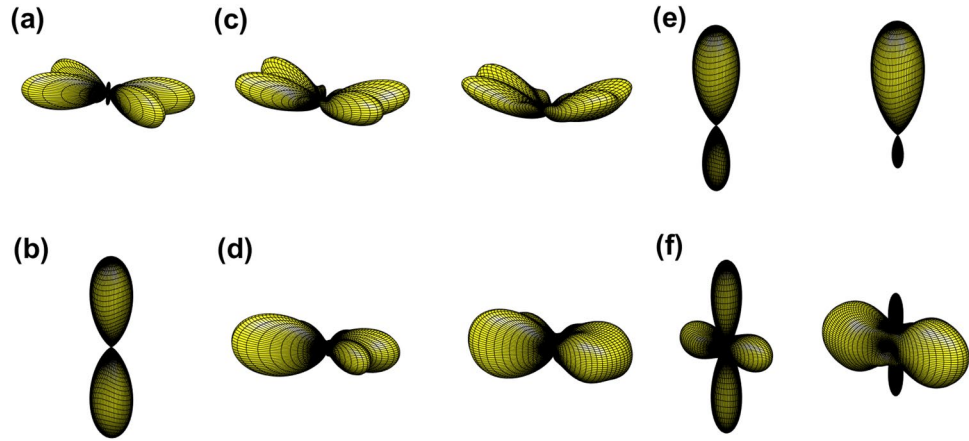


Figure 5. The far-field $\Omega_f(\theta, \phi)$ of \hat{x} -polarized HPI two-photon states for $N_\phi = 8$ and $N_{rz} = 1, 2$ and 3 in the stacked and concentric rings. For single ring, we plot two subradiant states (a) $l = 2$ and (b) $l = 4$ for comparisons. For stacked rings, the subradiant states with (c) $l = 2$ and (e) $l = 4$ are illustrated with $N_z = 2$ and 3 from left to right. Similarly for concentric rings, the subradiant (left) and superradiant (right) states respectively with (d) $l = 2$ and (f) $l = 4$ are illustrated with $N_r = 2$ and 3 from left to right. The viewing angle and other parameters are the same as in Fig. 2(a), and stacked ring separation $d_z/\lambda = 0.35$, concentric inter-ring distance $d_r/\lambda = 0.2$.

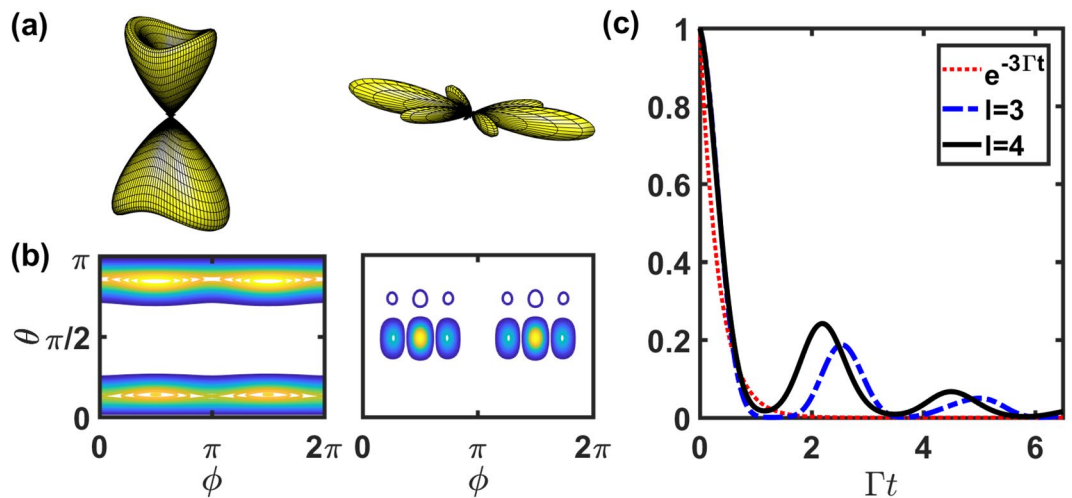


Figure 6. The far-field $\Omega_f(\theta, \phi)$ of \hat{x} -polarized HPI three-photon states for $N_\phi = 8$ and $N_z = 2$ in the stacked rings. The subradiant states with (a) $l = 3$ and $l = 4$ are illustrated from left to right with corresponding two-dimensional plots in (b). (c) The fluorescence intensity $I_0(t)$ of the HPI three-photon states compares with $e^{-3\Gamma t}$ (dot). The viewing angle and other parameters are the same as in Fig. 5.

For HPI three-photon subradiant states, we show the results of $\Omega_f(\theta, \phi)$ of two stacked rings in Fig. 6 as a comparison to Fig. 4. We find the enhanced oblique scattering toward the backward direction for $l = 3$ mode and narrowing side scattering peaks for $l = 4$ in polar angles θ . The small peaks at $\theta \approx 3\pi/4$ for $l = 4$ is also a signature of enhanced oblique scattering which breaks the mirror symmetry of the emission patterns in Fig. 4 with respect to $\hat{x} - \hat{y}$ plane. We note that the clear N_ϕ number of transverse scattering peaks disappear due to multiphoton effect. The time evolutions of these states in Fig. 6(c) shows the subradiant fluorescence, and the mode for $l = 3$ is more subradiant than the one in Fig. 4(c), which indicates the cooperative enhancement in subradiance when more atoms are stacked up. For more atoms, for example of $N_z = 3$, we find similar enhancement in oblique scattering and narrowing polar angle distribution for $l = 3$ and 4 modes respectively. For concentric rings, these three-photon modes do not show significant subradiance, similar to Fig. 5(c) and (d).

Discussion

Recently there is a huge advance in precisely controlling atomic separations in waveguide⁴⁴ or integrated color centers⁴⁵ and in assembling discrete atoms by optical microtraps^{46,47}, which has enabled fine tunings of light-matter interactions. These experimental techniques have promised an ultimate quantum control in quantum

optical systems. With well control of atomic configurations, we can manipulate RDDI of the spontaneous emission process. This controls the timescale of the emission, which makes subradiant states a resource for quantum memory. Subradiant far-field scattering, on the other hand, provides additional information for light collection and specific characterization of atomic geometry. This helps prepare genuine quantum states and makes quantum state engineering more efficient.

In conclusion, we propose to prepare the multiphoton subradiant states by imprinting the helical phases from OAM of light on the atoms in the stacked and concentric rings, and investigate their far-field scattering patterns. The directional scattering of the helical-phase-imprinted multiphoton subradiant states allows for light collimation, and their small spontaneous decay rates are preferential to quantum storage of light quanta with orbital angular momenta. We find enhanced forward (oblique backward) emission for HPI two (three)-photon subradiant states which can also support transverse scattering peaks. Therefore, we can tailor and control the scattering properties by engineering the atoms spatially, which essentially can facilitate quantum control of the many-body subradiant states and is useful in manipulating entanglement of large orbital angular momenta⁴⁸ or operating quantum gates⁴⁹.

Methods

Lindblad form of dissipation with resonant dipole-dipole interactions. The coupling matrix is based on the Lindblad forms of the spontaneous emissions. The general spontaneous emission process involves the dipole-dipole interaction⁴ which results from the rescattering events in the dissipation. For a quantum operator \hat{Q} , the Heisenberg equation in a Lindblad form reads

$$\frac{d\hat{Q}}{dt} = -i \sum_{\mu \neq \nu} \sum_{\nu=1}^N G_{\mu\nu} [\hat{Q}, \hat{\sigma}_{\mu}^{+} \hat{\sigma}_{\nu}^{-}] + \mathcal{L}_s[\hat{Q}], \quad (6)$$

where for the spontaneous emission,

$$\mathcal{L}_s[\hat{Q}] = - \sum_{\mu, \nu=1}^N \frac{F_{\mu\nu}}{2} (\hat{\sigma}_{\mu}^{+} \hat{\sigma}_{\nu}^{-} \hat{Q} + \hat{Q} \hat{\sigma}_{\mu}^{+} \hat{\sigma}_{\nu}^{-} - 2 \hat{\sigma}_{\mu}^{+} \hat{Q} \hat{\sigma}_{\nu}^{-}). \quad (7)$$

The dipole operator is $\hat{\sigma}_{\mu}^{-} (\hat{\sigma}_{\mu}^{+})$ where $\hat{\sigma}_{\mu}^{-} \equiv |g\rangle_{\mu} \langle e|$ and $\hat{\sigma}_{\mu}^{+} \equiv (\hat{\sigma}_{\mu}^{-})^{\dagger}$. The frequency shift $G_{\mu\nu}$ and decay rate $F_{\mu\nu}$ are⁴

$$F_{\mu\nu}(\xi) \equiv \frac{3\Gamma}{2} \left\{ [1 - (\hat{\mathbf{p}} \cdot \hat{\mathbf{r}}_{\mu\nu})^2] \frac{\sin \xi}{\xi} + [1 - 3(\hat{\mathbf{p}} \cdot \hat{\mathbf{r}}_{\mu\nu})^2] \left[\frac{\cos \xi}{\xi^2} - \frac{\sin \xi}{\xi^3} \right] \right\}, \quad (8)$$

$$G_{\mu\nu}(\xi) \equiv \frac{3\Gamma}{4} \left\{ -[1 - (\hat{\mathbf{p}} \cdot \hat{\mathbf{r}}_{\mu\nu})^2] \frac{\cos \xi}{\xi} + [1 - 3(\hat{\mathbf{p}} \cdot \hat{\mathbf{r}}_{\mu\nu})^2] \left[\frac{\sin \xi}{\xi^2} + \frac{\cos \xi}{\xi^3} \right] \right\}, \quad (9)$$

where Γ is the single-particle intrinsic decay rate of the excited state, $\xi = |\mathbf{k}_{\perp}| r_{\mu\nu}$, and the interparticle distance $r_{\mu\nu} = |\mathbf{r}_{\mu} - \mathbf{r}_{\nu}|$. The above expressions are valid for uniformly polarized excitations of the dipole \mathbf{p} .

References

- Dicke, R. H. Coherence in spontaneous radiation processes. *Phys. Rev.* **93**, 99–110 (1954).
- Gross, M. & Haroche, S. Superradiance: An essay on the theory of collective spontaneous emission. *Phys. Rep.* **93**, 301–396 (1982).
- Rehler, N. E. & Eberly, J. H. Superradiance. *Phys. Rev. A* **3**, 1735 (1971).
- Lehmberg, R. H. Radiation from an N -Atom System. I. General Formalism. *Phys. Rev. A* **2**, 883–888 (1970).
- Guerin, W., Araújo, M. O. & Kaiser, R. Subradiance in a large cloud of cold atoms. *Phys. Rev. Lett.* **116**, 083601 (2016).
- Mazets, I. E. & Kurizki, G. Multiatom cooperative emission following single-photon absorption: Dicke-state dynamics. *J. Phys. B: At. Mol. Opt. Phys.* **40**, F105–F112 (2007).
- Kimble, H. J. The quantum internet. *Nature* **453**, 1023–1030 (2008).
- Hammerer, K., Sørensen, A. S. & Polzik, E. S. Quantum interface between light and atomic ensembles. *Rev. Mod. Phys.* **82**, 1041 (2010).
- Scully, M. O. Single photon subradiance: quantum control of spontaneous emission and ultrafast readout. *Phys. Rev. Lett.* **115**, 243602 (2015).
- Jen, H. H., Chang, M.-S. & Chen, Y.-C. Cooperative single-photon subradiant states. *Phys. Rev. A* **94**, 013803 (2016).
- Sutherland, R. T. & Robicheaux, F. Collective dipole-dipole interactions in an atomic array. *Phys. Rev. A* **94**, 013847 (2016).
- Bettles, R. J., Gardiner, S. A. & Adams, C. S. Cooperative eigenmodes and scattering in one-dimensional atomic arrays. *Phys. Rev. A* **94**, 043844 (2016).
- Facchinetti, G., Jenkins, S. D. & Ruostekoski, J. Storing light with subradiant correlations in arrays of atoms. *Phys. Rev. Lett.* **117**, 243601 (2016).
- Jen, H. H. Cooperative single-photon subradiant states in a three-dimensional atomic array. *Ann. Phys. (N. Y.)* **374**, 27–34 (2016).
- Jen, H. H. Phase-imprinted multiphoton subradiant states. *Phys. Rev. A* **96**, 023814 (2017).
- Jenkins, S. D. & Ruostekoski, J. Metamaterial transparency induced by cooperative electromagnetic interactions. *Phys. Rev. Lett.* **111**, 147401 (2013).
- Jenkins, S. D., Ruostekoski, J., Papasimakis, N., Savo, S. & Zheludev, N. I. Many-body subradiant excitations in metamaterial arrays: Experiment and theory. *Phys. Rev. Lett.* **119**, 053901 (2017).
- DeVoe, R. G. & Brewer, R. G. Observation of superradiant and subradiant spontaneous emission of two trapped ions. *Phys. Rev. Lett.* **76**, 2049 (1996).
- Hettich, C. *et al.* Nanometer resolution and coherent optical dipole coupling of two individual molecules. *Science* **298**, 385 (2002).
- Takasu, Y. *et al.* Controlled production of subradiant states of a diatomic molecule in an optical lattice. *Phys. Rev. Lett.* **108**, 173002 (2012).
- McGuyer, B. H. *et al.* Precise study of asymptotic physics with subradiant ultracold molecules. *Nat. Phys.* **11**, 32 (2015).

22. Sonnefraud, Y. *et al.* Experimental realization of subradiant, superradiant, and Fano resonances in ring/disk plasmonic nanocavities. *ACS Nano* **4**, 1664 (2010).
23. Plankensteiner, D., Sommer, C., Ritsch, H. & Genes, C. Cavity antiresonance spectroscopy of dipole coupled subradiant arrays. *Phys. Rev. Lett.* **119**, 093601 (2017).
24. Röhlberger, R., Schlage, K., Sahoo, B., Couet, S. & Ruffer, R. Collective Lamb shift in single-photon superradiance. *Science* **328**, 1248–1251 (2010).
25. Keaveney, J. *et al.* Cooperative Lamb shift in an atomic vapor layer of nanometer thickness. *Phys. Rev. Lett.* **108**, 173601 (2012).
26. Meir, Z., Schwartz, O., Shahmoon, E., Oron, D. & Ozeri, R. Cooperative Lamb Shift in a mesoscopic atomic array. *Phys. Rev. Lett.* **113**, 193002 (2014).
27. Pellegrino, J. *et al.* Observation of suppression of light scattering induced by dipole-dipole interactions in a cold-atom ensemble. *Phys. Rev. Lett.* **113**, 133602 (2014).
28. Jennewein, S. *et al.* Coherent scattering of near-resonant light by a dense microscopic cold atomic cloud. *Phys. Rev. Lett.* **116**, 233601 (2016).
29. Roof, S. J., Kemp, K. J., Havey, M. D. & Sokolov, I. M. Observation of single-photon superradiance and the cooperative Lamb shift in an extended sample of cold atoms. *Phys. Rev. Lett.* **117**, 073003 (2016).
30. Bromley, S. L. *et al.* Collective atomic scattering and motional effects in a dense coherent medium. *Nat. Commun.* **7**, 11039 (2016).
31. Zhu, B., Cooper, J., Ye, J. & Rey, A. M. Light scattering from dense cold atomic media. *Phys. Rev. A* **94**, 023612 (2016).
32. Shahmoon, E., Wild, D. S., Lukin, M. D. & Yelin, S. F. Cooperative resonances in light scattering from two-dimensional atomic arrays. *Phys. Rev. Lett.* **118**, 113601 (2017).
33. Jen, H. H., Chang, M.-S. & Chen, Y.-C. Cooperative light scattering from helical-phase-imprinted atomic rings. arXiv 1801.00559.
34. Arnaut, H. H. & Barbosa, G. A. Orbital and intrinsic angular momentum of single photons and entangled pairs of photons generated by parametric down-conversion. *Phys. Rev. Lett.* **85**, 286 (2000).
35. Mair, A., Vaziri, A., Weihs, G. & Zeilinger, A. Entanglement of Orbital Angular Momentum States of Photons. *Nature* **412**, 313–316 (2001).
36. Molina-Terriza, G., Torres, J. P. & Torner, L. Twisted photons. *Nat. Phys.* **3**, 305–310 (2007).
37. Dada, C. *et al.* E. Experimental high-dimensional two-photon entanglement and violations of generalized Bell inequalities. *Nat. Phys.* **7**, 677–680 (2011).
38. Fickler, R. *et al.* Quantum entanglement of high angular momenta. *Science* **338**, 640–643 (2012).
39. Nicolas, A. *et al.* A quantum memory for orbital angular momentum photonic qubits. *Nat. Photonics* **8**, 234–238 (2014).
40. Ding, D.-S. *et al.* Quantum storage of orbital angular momentum entanglement in an atomic ensemble. *Phys. Rev. Lett.* **114**, 050502 (2015).
41. Zhou, Z.-Q. *et al.* Quantum storage of three-dimensional orbital-angular-momentum entanglement in a crystal. *Phys. Rev. Lett.* **115**, 070502 (2015).
42. Olmos, B. & Lesanovsky, I. Collective photon emission from symmetric states created with Rydberg atoms on a ring lattice. *Phys. Rev. A* **82**, 063404 (2010).
43. Pan, J.-W. *et al.* Multiphoton entanglement and interferometry. *Rev. Mod. Phys.* **84**, 777 (2012).
44. Goban, A. *et al.* Superradiance for atoms trapped along a photonic crystal waveguide. *Phys. Rev. Lett.* **115**, 063601 (2015).
45. Sipahigil, A. *et al.* An integrated diamond nanophotonics platform for quantum-optical networks. *Science* **354**, 847–850 (2016).
46. Barredo, D., de Léséleuc, S., Lienhard, V., Lahaye, T. & Browaeys, A. An atom-by-atom assembler of defect-free arbitrary two-dimensional atomic arrays. *Science* **354**, 1021–1023 (2016).
47. Endres, M. *et al.* Atom-by-atom assembly of defect-free one-dimensional cold atom arrays. *Science* **354**, 1024–1027 (2016).
48. Fickler, R., Campbell, G., Buchler, B., Lam, P. K. & Zeilinger, A. Quantum entanglement of angular momentum states with quantum numbers up to 10,010. *Proc. Natl. Acad. Sci. USA* **113**, 13642–13647 (2016).
49. Babazadeh, A. *et al.* High-dimensional single-photon quantum gates: Concepts and experiments. *Phys. Rev. Lett.* **119**, 180510 (2017).

Acknowledgements

This work is supported by the Ministry of Science and Technology (MOST), Taiwan, under the Grant No. MOST-106-2112-M-001-005-MY3. H.H.J. is partially supported by a grant from MOST of No. 106-2811-M-001-130, as an assistant research scholar in IOP, Academia Sinica. We are also grateful for the support of NCTS ECP1 (Experimental Collaboration Program) and for stimulating discussions with M.-S. Chang and Y.-C. Chen.

Author Contributions

H.H. Jen conducted the derivations and numerical simulations, analyzed the results, and wrote the manuscript.

Additional Information

Competing Interests: The author declares no competing interests.

Publisher's note: Springer Nature remains neutral with regard to jurisdictional claims in published maps and institutional affiliations.



Open Access This article is licensed under a Creative Commons Attribution 4.0 International License, which permits use, sharing, adaptation, distribution and reproduction in any medium or format, as long as you give appropriate credit to the original author(s) and the source, provide a link to the Creative Commons license, and indicate if changes were made. The images or other third party material in this article are included in the article's Creative Commons license, unless indicated otherwise in a credit line to the material. If material is not included in the article's Creative Commons license and your intended use is not permitted by statutory regulation or exceeds the permitted use, you will need to obtain permission directly from the copyright holder. To view a copy of this license, visit <http://creativecommons.org/licenses/by/4.0/>.

© The Author(s) 2018